www.ietdl.org

Published in IET Power Electronics
Received on 5th July 2012
Revised on 16th October 2012
Accepted on 8th November 2012
doi: 10.1049/iet-pel.2012.0329

ISSN 1755-4535

Low computational burden grid voltage sensorless current controller

Sebastian Gomez Jorge, Claudio Alberto Busada, Jorge Solsona

Instituto de Investigaciones en Ingeniería Eléctrica, Departamento de Ingeniería Eléctrica y de Computadoras, Universidad Nacional del Sur – CONICET, Avda. Alem 1253, (8000) Bahía Blanca, Argentina
E-mail: sebastian.gomezjorge@uns.edu.ar

Abstract: This study proposes a grid voltage sensorless reduced order generalised integrator-based current controller. The proposal takes advantage of the controller structure to avoid the grid voltage measurement, avoiding the need of additional states and requiring only a few multiply and add operations for its computation. This allows one to keep the controller's computational burden to a minimum, making it ideal for low cost digital signal processor implementation.

1 Introduction

In recent years, there has been an increasing trend towards the use of distributed power generation systems (DPGS) [1]. They have been used for stand alone generation as well as for supplying power to the mains grid [2–5]. One of the main components of a DPGS is the voltage source converter (VSC), and many strategies have been proposed to control it. The basic number of sensors required to implement a three-phase VSC controller is usually five (two ac phase current sensors, two ac phase voltage sensors, and the dc-link voltage sensor). In order to reduce the system's cost and increase its reliability, it is desirable to use the minimum number of sensors. An often used approach is to eliminate the grid voltage sensor. Many grid voltage sensorless control strategies have been proposed, some of which are reviewed in what follows.

The authors of [6] propose a grid voltage sensorless control scheme for a DPGS assuming the grid as an L–R system whose parameters are unknown. These are estimated through parameter adaptation performed measuring only the grid current, and using a neural network (NN) the grid voltage is estimated. The current control is performed in a synchronous frame using the deadbeat technique, and the synchronisation is achieved by means of a phase locked loop (PLL). Although the proposal shows good performance, it is only tested for a pure sinusoidal grid voltage. Also, its implementation in digital signal processor (DSP) has a relatively high computational burden, which limits the VSC switching frequency to 6.7 kHz. This can result in the requirement of larger coupling inductors to achieve reduced current ripples. In [7] a stand alone DPGS grid voltage sensorless control strategy is proposed. Here, a Kalman filter is used to predict the control state variables one sample ahead using only the system parameters and the grid current measurement. This is done to compensate the one sample delay introduced by the DSP. The grid voltage control is performed using a second order generalised integrator (SOGI) [8] and the current control is simply performed through a proportional controller. Three different feedback schemes are analysed, and it is concluded that using the coupling filter capacitor current provides enhanced stability. This allows a higher controller bandwidth. However, the effects of nonlinear load are not analysed, and both simulation and experimental results are provided for a linear load. In [9] a grid connected DPGS control scheme is proposed. Here, a similar grid voltage estimation scheme using Kalman filter is used. The control is performed through a proportional-integral (PI) controller implemented in a synchronous frame, which is synchronised by means of a PLL. The stability of the system to four different feedback schemes is analysed, and it is concluded that using the coupling capacitor current yields the best stability properties. Robustness of the proposal to parameter variation is also verified. However, the system is only tested when in presence of a pure sinusoidal grid voltage. The authors of [10] use flatness to control a grid connected VSC. Using nonlinear model-based observers the grid voltage is estimated, which results in a sensorless control scheme. The synchronisation is provided by these observers. Robustness to parameter uncertainties and grid voltage voltage sags is verified. However, proposal is only tested for a pure sinusoidal grid voltage. In [11] a NN is used to estimate a signal that represents the grid voltage disturbance and the parametric uncertainties of the system. This signal is used to perform the grid voltage sensorless control of a grid connected DPGS. A synchronous frame dead beat control is implemented, and the grid synchronisation is performed using a PLL and a SOGI-based filter. As in [6], the DSP implementation has relatively high computational cost, resulting in a switching frequency of 6.7 kHz.

Most of the previously described strategies require a relatively high computational power to be performed. If the

control scheme is to be implemented in a very low cost DSP, the computational burden must be further reduced. A very low computational burden a three-phase current controller is proposed in [12]. This controller is based on the reduced order generalised integrator (ROGI). The main characteristic of the ROGI is that it is sensitive to both, frequency and sequence, which allows, in low imbalance grids, to reduce the computational burden of the controller. The performance of this ROGI-based controller is similar to that of SOGI or adaptive notch filter-based ones. Its main advantage is of computational nature, making it ideal for low cost DSP implementation. Another important feature of this scheme is that it does not require knowledge of the fundamental component of the grid voltage in order to produce balanced high quality injected currents. This eliminates the need of a synchronisation scheme, further reducing the computational burden of the implementation.

This paper proposes a grid voltage sensorless version of the ROGI-based current controller. Its main features are the following:

- It allows one to avoid measuring the grid voltage, there by saving on hardware (sensors, signal conditioning, analog-to-digital converters etc.).
- Its implementation requires the same number of states as the controller with grid voltage sensor, and increases its computational cost only in a reduced number of multiply and add operations. These additional operations are further justified in the time saved by avoiding the capture, scaling and transforming to the alpha–beta stationary frame of two grid voltages.
- It performs similarly to the ROGI-based controller with grid voltage sensor, having the same capability of producing high quality steady-state currents.

Furthermore, it will be shown that the proposal is not significantly affected by coupling inductance deviation from its nominal value.

The paper is organised as follows. In Section 2 a description of the system and its discrete time model are given. Section 3 briefly describes the existing ROGI-based current controller. Section 4 describes the proposed sensorless scheme. In Sections 5 and 6 simulation and experimental results are shown, respectively. Finally, in Section 7 conclusions are drawn.

2 System description

Fig. 1 shows the system to be controlled. In this figure, the VSC is composed of a primary source, which supplies the power, and a three legged inverter. This converter is connected to the grid through the coupling inductances L, and controls the injected phase currents i_{sa}, i_{sb} and i_{sc}. The grid voltages are represented by the voltage sources v_{sa}, v_{sb} and v_{sc}, respectively. The VSC gate signals are generated through a digital signal processor (DSP), represented in the figure by the block 'Controller'. In order to compute the control signals, this DSP requires, in principle, measurements of two-phase currents, the VSC bus voltage and two grid line voltages. Later, when the grid voltage sensorless strategy is developed, the line voltage sensors will not be needed.

Fig. 2 shows a discrete time model of the system. Here, the block 'Plant' represents the discrete time model of the coupling inductors, and for convenience, the DSP

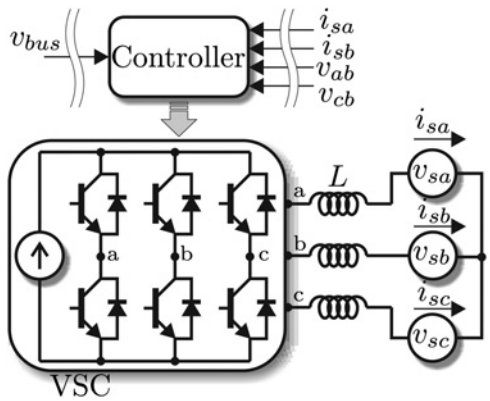

Fig. 1 *System description*

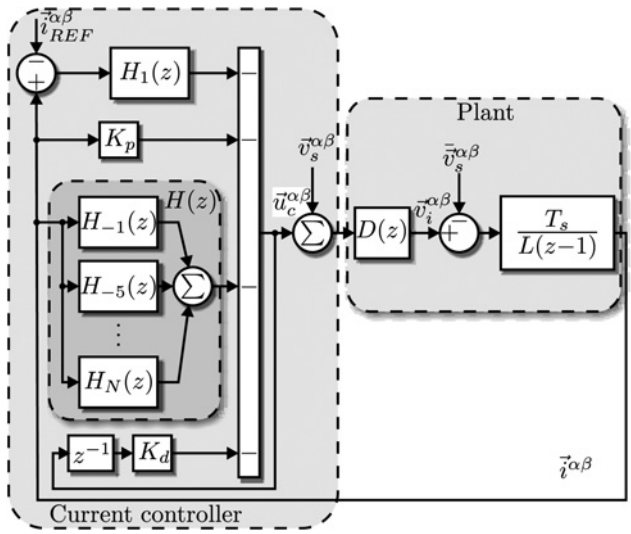

Fig. 2 *Plant/controller discrete time model*

processing delay has also been included. The behaviour of the coupling inductances is modelled through the zero-order hold discretisation of their differential equations, which results in the transfer function shown in the figure. In this model the variables are complex space vectors, represented in the stationary reference frame [13, 14], which is denoted by the superscript $\alpha\beta$. These variables are the grid current $\vec{i}^{\alpha\beta}$, the converter voltage $\vec{v}_{\mathrm{i}}^{\alpha\beta}$ (which is applied to the coupling inductors) and the control signal $\vec{u}_{\mathrm{c}}^{\alpha\beta}$. The control signal is applied to the coupling inductors through the VSC after the DSP processing delay, which is defined as

$$D(z) = d_1 + d_2 z^{-1} \tag{1}$$

where $d_1 = 1 - \tau/T_{\mathrm{s}}$ and $d_2 = \tau/T_{\mathrm{s}}$, with T_{s} the sampling time and $\tau \leq T_{\mathrm{s}}$ the processing delay time [12]. The grid voltage $\vec{v}_{\mathrm{s}}^{\alpha\beta}$ and the VSC nonlinearities $\vec{v}_{\mathrm{nl}}^{\alpha\beta}$ (usually dead time and collector–emitter voltage drops) have been grouped together in the signal $\bar{\vec{v}}_{\mathrm{s}}^{\alpha\beta} = \mathrm{mean}(\vec{v}_{\mathrm{s}}^{\alpha\beta} + \vec{v}_{\mathrm{nl}}^{\alpha\beta})\big|_{T_{\mathrm{s}}}$, which is the sum of both signals averaged over a DSP sampling period T_{s}. The block 'Current control' shown in Fig. 2 is responsible for generating the control signal, and will be discussed in detail in the following section.

3 Current control strategy description

The objective of most DPGS current controllers is the injection of balanced sinusoidal currents of fundamental

frequency with a low total harmonic distortion (THD). To this end, the controller must be able to both track the fundamental component of the grid voltage and reject its main harmonic components. This can be easily achieved by means of a ROGI-based current controller [12]. In balanced systems, this controller results in a very low computational burden implementation, and does not require any external synchronisation algorithm to track the phase of the fundamental component of the grid voltage.

A ROGI-based controller is shown in the block 'Current controller' of Fig. 2. In the figure, the ROGIs are represented by the transfer functions $H_h(z)$, where

$$H_h(z) = \frac{K_h}{z - \mathrm{e}^{h\mathrm{j}\omega_o T_s}} \tag{2}$$

with $h \in \mathbb{Z}$, $\mathrm{j} = \sqrt{-1}$, $K_h \in \mathbb{C}$ a design constant and ω_o the nominal fundamental grid angular frequency. Fig. 3 shows the Bode plot of $H_1(\mathrm{e}^{\mathrm{j}\omega T_s})$ for $K_1 = 1$. Here, positive frequencies show the response to a positive sequence input vector, and negative frequencies to a negative sequence one. As can be seen, the ROGIs are resonant discrete filters sensitive to both frequency and sequence that provide an infinite gain at the frequencies at which they are tuned to. In this case, for $H_1(z)$, that frequency is ω_o. The internal model principle (IMP) states that if the frequency modes of the reference and the disturbances to reject are included in the control loop, then the steady-state error will not contain these frequencies [15]. For example an analog PI controller is based on the IMP: the presence in the loop of the pole at $s = 0$ ensures that the system is able to track without steady-state error a dc signal, even in presence of a dc disturbance. The IMP ensures that placing ROGIs in a feedback loop of the grid current will eliminate from this current the harmonic sequences at which they are tuned to. In Fig. 2 the harmonic compensation is performed by the transfer function

$$H(z) = \sum_{\substack{h = -1, -5, \ldots, N \\ h \neq 1}} H_h(z) \tag{3}$$

which is placed in a feedback loop of the injected current $i^{\alpha\beta}$. This means that, in steady-state, this current cannot have any harmonic of orders $h = -1, -5, \ldots, N$. Also, since the error between the reference current $\vec{i}^{\alpha\beta}_{\mathrm{REF}}$ and the actual current $\vec{i}^{\alpha\beta}$ is feeded to the ROGI $H_1(z)$, it is clear, from the IMP, that $i^{\alpha\beta}$ will track the fundamental component of $\vec{i}^{\alpha\beta}_{\mathrm{REF}}$ without error. Note that even if the reference current has harmonics, if there are ROGIs tuned at those harmonic orders in $H(z)$ then their perturbation effect will be compensated by the controller. If the control objective is to inject sinusoidal currents in phase with the fundamental component of the grid voltage, the features of the ROGI-based controller allow one to avoid the need for an additional synchronisation algorithm, reducing the overall computational burden. For unity power factor, the reference current can simply be chosen as a scaled version of the measured grid voltage

$$\vec{i}^{\alpha\beta}_{\mathrm{REF}}(k) = g\vec{v}^{\alpha\beta}_{\mathrm{s}}(k) \tag{4}$$

where $g \in \mathbb{R}$, $g > 0$ is a scalar that determines the magnitude of the injected current, and $\vec{v}^{\alpha\beta}_{\mathrm{s}}(k)$ is the actual measured grid voltage. The gain g usually comes from an external control loop which is tasked to extract the maximum power from the primary source. The description of this external control loop escapes the scope of this paper, and therefore from now on g will be assumed a known given constant. In Fig. 2, the measured grid voltage is also sent feed-forward to the output of the controller. This term is included in order to improve the current transient response when in presence of sudden grid voltage variations.

The controller gains K_h perform a full-state feedback. Since the current $\vec{i}^{\alpha\beta}$ is a system state and the processing delay can be modelled as an additional state, these signals have their associated gains, which in Fig. 2 are K_p and K_d, respectively. These gains can be found using a pole placement linear control technique such as the linear quadratic regulator (LQR) method, assuming that the coupling inductances value $L = \hat{L}$, where $\hat{L}$ is their nominal value.

Despite the features described so far, the ROGI-based current controller requires the measurement of the grid voltage, as shown in (4). This measurement is critical for the performance of the controller, since it provides information about the shape of the reference current and also the phase to which this current must be synchronised. Therefore in order to increase the system's reliability and reduce its cost, it is of interest to develop a way to avoid its use.

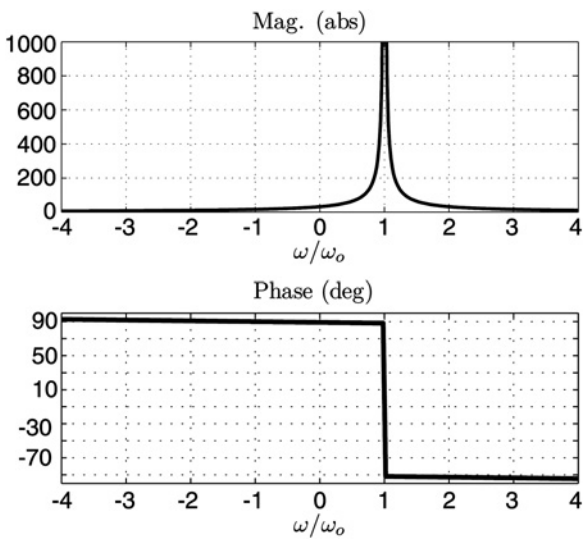

Fig. 3 *ROGI $H_1(e^{j\omega T_s})$ Bode plot*

4 Grid voltage sensorless controller

In this section we will show how to make the current controller described in Section 3 a grid voltage sensorless controller. This will allow one to eliminate the need of the line voltage measurements shown in Fig. 1, which reduces cost and also increases the reliability of the system. The proposed sensorless scheme requires no additional states, and very few additional operations. This results in a low computational burden control algorithm. The controller will result capable of synthesizing balanced sinusoidal currents, in phase with the positive sequence fundamental component of the grid voltage.

4.1 Sensorless strategy

In the controller shown in Fig. 2, the measured grid voltage is feed-forwarded to the output of the controller to improve its

IET Power Electron., 2013, Vol. 6, Iss. 8, pp. 1592–1599
doi: 10.1049/iet-pel.2012.0329

dynamic response to sudden variations in the grid voltage. In order to perform the sensorless scheme, we will remove the feed-forward term. The price paid for the sensorless implementation will be therefore a slower transient response of the current controller when in presence of grid voltage variations.

As was described in Section 3, the measurement of the grid voltage $\vec{v}_s^{\alpha\beta}(k)$ is required in order to compute the reference current (4). However, this voltage does not explicitly appear in the discrete time model shown Fig. 2. Instead $\bar{\vec{v}}_s^{\alpha\beta}$ is used. This signal represents the sum of the grid voltage and the VSC nonlinearities, averaged over a sample period T_s. In this paper, the control objective will be to force the current to track the reference current given by

$$\vec{i}_{REF}^{\alpha\beta}(k) = g\bar{\vec{v}}_s^{\alpha\beta}(k) \tag{5}$$

instead of (4) as in the conventional ROGI-based controller. This is a valid approach, since the most significant voltage drop of the VSC nonlinearities $\vec{v}_{nl}^{\alpha\beta}$ is caused by the dead times and semiconductor voltage drops, which result in a wave whose fundamental frequency component is in phase with the phase currents, and thus, does not introduce any phase error between the injected currents and the grid voltage when both are in phase. From Fig. 2, removing the feed-forward grid voltage and assuming the coupling inductors at their nominal value ($L = \hat{L}$), $\bar{\vec{v}}_s^{\alpha\beta}$ could in principle be estimated from the following transfer function

$$\bar{\vec{v}}_s^{\alpha\beta} = \vec{v}_i^{\alpha\beta} - \frac{\hat{L}(z-1)}{T_s}\vec{i}^{\alpha\beta} \tag{6}$$

where

$$\vec{v}_i^{\alpha\beta} = D(z)\vec{u}_c^{\alpha\beta} \tag{7}$$

or written as a difference equation

$$\bar{\vec{v}}_s^{\alpha\beta}(k) = \underbrace{\vec{v}_i^{\alpha\beta}(k)}_{\text{inverter voltage}} \underbrace{-\frac{\hat{L}}{T_s}\left(\underbrace{\vec{i}^{\alpha\beta}(k+1)}_{\text{noncausal}} - \vec{i}^{\alpha\beta}(k)\right)}_{\text{inductor voltage}} \tag{8}$$

Note that this is a noncausal difference equation, since it requires knowledge of the future sampled current $\vec{i}^{\alpha\beta}(k+1)$. However, all the other values required to compute it are readily available, since writing (7) as a difference equation, it results

$$\vec{v}_i^{\alpha\beta}(k) = d_1\vec{u}_c^{\alpha\beta}(k) + d_2\vec{u}_c^{\alpha\beta}(k-1) \tag{9}$$

which is computed using the actual value of control signal and its previous value, that is available since it is used in the full-state feedback. In what follows, taking advantage of the controller's structure, we will avoid the need for the future sample of the measured current. To do so, we will first replace (8) in (5), and then group all the readily available signals into a single term, which enables us to rewrite the reference current as

$$\vec{i}_{REF}^{\alpha\beta}(k) = \vec{r}(k) - g\frac{\hat{L}}{T_s}\vec{i}^{\alpha\beta}(k+1) \tag{10}$$

where $\vec{r}(k) = g\vec{v}_i^{\alpha\beta}(k) + g(L/T_s)\vec{i}^{\alpha\beta}(k)$. Fig. 4*a* shows a block diagram description of the fundamental ROGI H_1. From the figure, the difference equation that relates the input $\vec{i}_{REF}^{\alpha\beta}(k)$ with the output $\vec{y}_1$ is

$$\vec{y}_1(k+1) = \vec{i}^{\alpha\beta}(k) - \vec{i}_{REF}^{\alpha\beta}(k) + e^{j\omega_o T_s}\vec{y}_1(k) \tag{11}$$

Now, replacing (10) in this equation, subtracting $g\frac{\hat{L}}{T_s}\vec{i}^{\alpha\beta}(k+1)$ both sides of the resulting equation, and defining the auxiliary signal

$$\vec{f}(k) = \vec{y}_1(k) - g\frac{\hat{L}}{T_s}\vec{i}^{\alpha\beta}(k) \tag{12}$$

Equation (11) can be rewritten as

$$\vec{f}(k+1) = \vec{i}^{\alpha\beta}(k) - \vec{r}(k) + e^{j\omega_o T_s}\left[\vec{f}(k) + g\frac{\hat{L}}{T_s}\vec{i}^{\alpha\beta}(k)\right] \tag{13}$$

Note that the computation of (13) does not require knowledge of the future sample of the measured current. Moreover, the output $\vec{y}_1$ of the fundamental ROGI H_1 can be easily reconstructed from (12). Replacing the fundamental ROGI H_1 (Fig. 4*a*) by these two equations, the controller can force the injected current to track the reference current (5) without actually measuring the grid voltage, and without requiring the future sample of this grid current either. Fig. 4*b* shows a block diagram representation of (13), and Fig. 5 shows the block diagram of the proposed sensorless current controller which results from replacing the ROGI H_1 in Fig. 2 with the implementation of Fig. 4*b*, and removing the grid voltage feed-forward term. From Fig. 5 it is also easy to see that the sensorless proposal adds a total of eight products (d_1, d_2, g and $g\hat{L}/T_s$) and six sums to the implementation of the controller (remember that each signal is complex), which is clearly a negligible additional computational burden.

Remark. In applications where the instantaneous grid voltage is required (e.g. for anti-islanding purposes), a one sample delayed version of (8) can be used to estimate its value. To use this equation in a practical application, the voltage drop produced by the VSC dead times should be taken into consideration. A rough approximation of the this voltage drop is the square wave given by [16]

$$\boldsymbol{v}_{dt}(k-1) = \frac{T_{dt}}{T_{pwm}}v_{bus}\ \mathrm{sign}\left(\boldsymbol{i}^{abc}(k-1)\right) \tag{14}$$

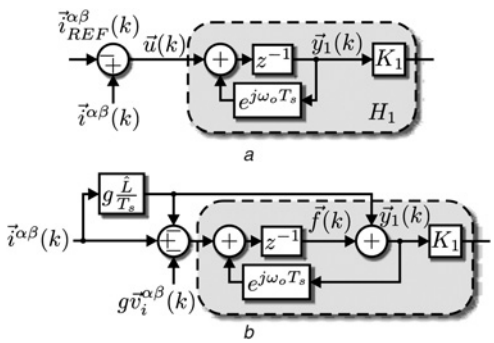

Fig. 4 *ROGI structure*

a Fundamental ROGI
b Grid voltage sensorless ROGI

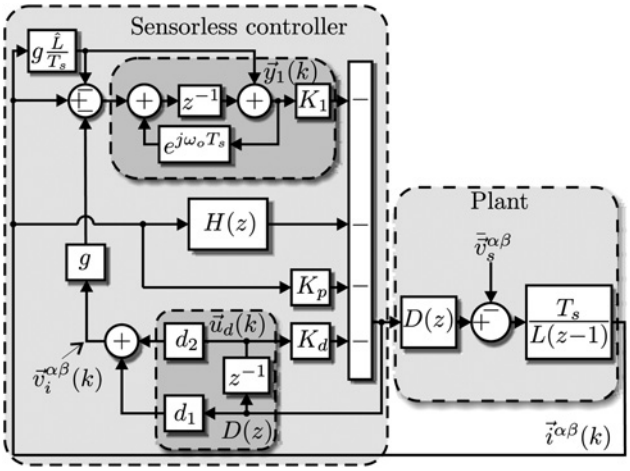

Fig. 5 *Sensorless current controller*

where T_{dt} is the dead time in seconds, T_{pwm} is the VSC switching period, v_{bus} is the dc link voltage and $\boldsymbol{i}^{abc} = [i_{sa} i_{sb} i_{sc}]^T$. To obtain a good estimation of the grid voltage, (8) should be anti-transformed to the *abc* frame through the inverse Clarke transform $\boldsymbol{T}_{\alpha\beta/abc}$, and (14) should be subtracted from it, which results in

$$\hat{\vec{v}}_s^{abc}(k-1) = \boldsymbol{T}_{\alpha\beta/abc}\vec{v}_s^{\alpha\beta}(k-1) - \boldsymbol{v}_{dt}(k-1) \qquad (15)$$

that is the estimated phase voltage, where $\hat{\vec{v}}_s^{abc} = [\hat{v}_{sa}\hat{v}_{sb}\hat{v}_{sc}]^T$.

4.2 Proposal validation and inductance variation robustness

In order to formally show that the proposed sensorless controller of Fig. 5 is capable of producing perfectly sinusoidal balanced currents of unity power factor, even when in presence of unbalanced and harmonic contaminated grid voltages, the frequency response method will be used. To this end, the magnitude of the frequency response of the transfer function

$$G(z) = \frac{\vec{i}^{\alpha\beta}(z)}{\vec{v}_s^{\alpha\beta}(z)} \qquad (16)$$

which is obtained for the controller structure described in Table 1, has been plotted, normalised by g, in Fig. 6*a*. This response was obtained evaluating $G(e^{j\omega T_s})$. The obtention of this transfer function is described in the appendix. As the figure shows, the injected current tracks the fundamental positive sequence component of $\vec{v}_s^{\alpha\beta}$ since $|\vec{i}^{\alpha\beta}(e^{j\omega_o T_s})|/(g|\vec{v}_s^{\alpha\beta}(e^{j\omega_o T_s})|) = 1$, where ω_o is the nominal grid frequency. This figure also shows that the sensorless controller is also capable of rejecting the sequences present in $\vec{v}_s^{\alpha\beta}$ which were modelled in the harmonic compensator $H(z)$ ($h = -1, -5, 7, -11, 13, -17, 19, \ldots$). This proves that, in steady-state, the sensorless controller is capable of injecting balanced currents with low distortion.

Since the sensorless scheme requires knowledge of the coupling inductor nominal value $\hat{L}$ to compute the gain $g\hat{L}/T_s$ shown in Fig. 5, we will now show the robustness of the controller to a mistuning in this parameter. Figs. 6*b* and *c* show a zoomed version of the magnitude and phase of the frequency response of (16), respectively. Here, we have

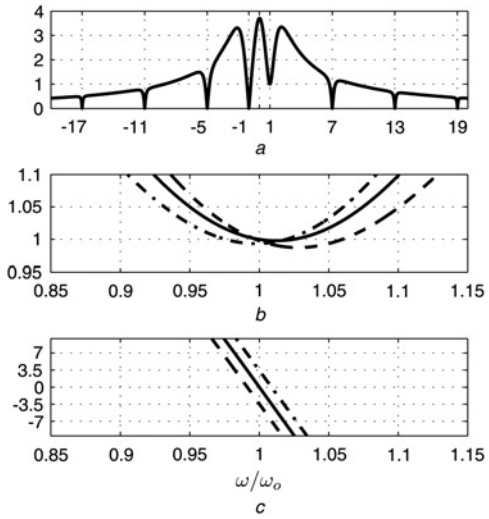

Fig. 6 *Sensorless frequency response for $L = \hat{L}$ (solid), $L = 0.5\hat{L}$ (dashed) and $L = 1.5\hat{L}$ (dashed/dot)*
a $|G(e^{j\omega T_s})|/g$
b $|G(e^{j\omega T_s})/g|$ (zoomed)
c $\arg(G(e^{j\omega T_s})$ (zoomed)

superimposed the plots of three different frequency responses. With solid line, the frequency response when L in the block 'Plant' of Fig. 5 equals its nominal value $\hat{L}$, which is given in Table 1; with dashed line, the frequency response when the plant inductor $L = 0.5\hat{L}$, and with dashed/dot line, the frequency response when the plant inductor $L = 1.5\hat{L}$. In all these plots, both the value of L in the block 'Sensorless controller' of Fig. 5 and the feedback gains K_h were kept fixed at their nominal values ($\hat{L}$ and the gains obtained for this inductor value, respectively). As Fig. 6*b* shows, the positive sequence fundamental component magnitude tracking capabilities of the controller are not significantly affected by the inductor mistuning. Fig. 6*c* shows that there is a slight phase tracking error when in presence of inductor mistuning. However, this error is less than 3.6° (200 µs for a fundamental angular frequency $\omega_o = 2\pi 50$ Hz) for a ±50% mistuning, which is rather acceptable for such a large parameter mistune. Although it is not shown in these two last plots for space reasons, the harmonic rejection capabilities of the controller remain unaltered when in presence of inductor mistuning. These results show that the sensorless controller is not only able to fulfill the control goals, but also that it is highly robust to L mistuning.

5 Simulation results

To show the robustness of the sensorless controller and its transient response when in presence of grid voltage variations, a grid voltage that goes from the lowly distorted grid voltage described in Table 2(a) (THD = 5.06%) to the highly distorted grid voltage described in Table 2(b) (THD = 53.6%) was simulated. A harmonic $h = -1$ (28.6%) was also added when the highly distorted grid voltage is applied. The nominal frequency was set to $\omega_o = 2\pi 50$ Hz and the nominal fundamental component voltage to 100 Vrms. The controller structure and parameters are shown in Table 1. The DSP processing delay was set to $\tau = T_s/2$ in order to simulate an actual VSC PWM update period of $T_s/2$. Also, the current reference gain goes from

IET Power Electron., 2013, Vol. 6, Iss. 8, pp. 1592–1599
doi: 10.1049/iet-pel.2012.0329

Table 1 Simulation/experimental system setup

Symbol	Value	Reference
h	1, −1, −5, 7, −11, 13, −17, 19, −23, 25	ROGIs
T_s	100 μs	sample time
τ	$T_s/2$	DSP delay
T_{pwm}	50 μs	PWM period
$L = L$	5.5 mH	coupling ind.
g	0.07 A/V	current gain
$\boldsymbol{Q}$	diag ([100 100 1 1 1 1 1 1 1 1 1 1])	LQR $\boldsymbol{Q}$ matrix
R	10	LQR R scalar
T_{dt}	1 μs	dead time
v_{ce}	1.5 V	IGBT V drop
v_d	1 V	diode V drop
v_{bus}	550 V	bus voltage

Table 2 Test voltages (% of fundamental component)

	(a) THD = 5.06%	(b) THD = 53.6%
V_{-5}	3.5	34.1
V_7	3.5	27.3
V_{-11}	1	20.4
V_{13}	0.25	20.4
V_{-17}	0	10
V_{19}	0	5
V_{-23}	0	1
V_{25}	0	1

zero to $g = 0.07$ A/V at simulation time 0.36 s. This is to show that the controller has good transient response to reference current changes. With the chosen final value of g, the injected current results 7 Arms per phase. The nonlinearities of the VSC were modelled through dead time, IGBT collector–emitter voltage drop and reverse diode voltage drop, according to Table 1. The switching of the IGBTs was also simulated.

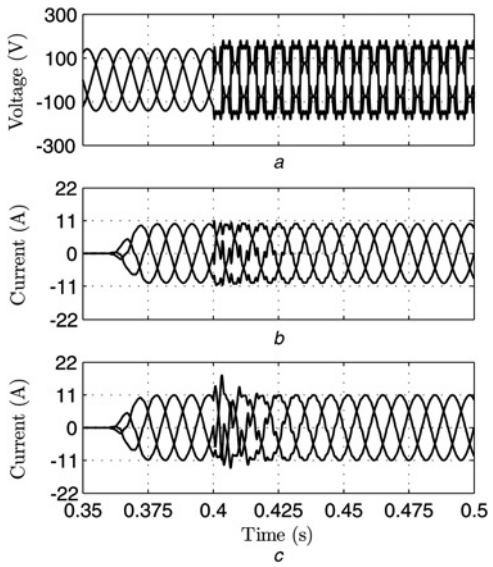

Fig. 7 *Simulation results in presence of a distorted voltage*

a Grid voltage
b Injected current (measuring grid voltage)
c Injected current (sensorless)

Fig. 7*a* shows the grid voltage, which goes from the balanced grid voltage described in Table 2(a) to the distorted grid voltage of Table 2(b) (plus the −1 imbalance) at simulation time 0.4 s. For comparison, Fig. 7*b* shows the currents injected by the current controller shown in Fig. 2, which uses the measured grid voltage $\bar{v}_s^{\alpha\beta}(k)$ to synthesize the reference current (4). As can be seen, injected currents are almost pure balanced sinusoids in steady-state. The steady-state THD of these currents is 0.57%, and its amplitude is 7 Arms. Finally, Fig. 7*c* shows the currents injected by the sensorless current controller shown in Fig. 5. The steady-state THD of these currents is 0.52% and its amplitude is 7.49 Arms. The difference between the magnitude of the injected currents for the standard and sensorless controllers is because of the nonlinearities of the VSC. In effect, for the sensorless controller, the reference current (5) is a scaled version of $\bar{\bar{v}}_s^{\alpha\beta}$, which the sum of the grid voltage and the VSC nonlinearities, whose fundamental component results larger than that of the grid voltage $\bar{v}_s^{\alpha\beta}$ used in (4). Fig. 7 also shows that even though the startup transients of both controllers are similar, there is a noticeable difference between the transient performances when in presence of a grid voltage variation. This difference is because of the fact that the sensorless controller does not have the feed-forward term $\bar{v}_s^{\alpha\beta}(k)$ at its output, that is present in the conventional ROGI-based controller shown in Fig. 2. The slower transient response of the sensorless controller is the price paid for an increased system reliability and implementation cost reduction. However, these simulations show that the sensorless controller works as good as the nonsensorless one, in steady-state.

6 Experimental results

The controller was implemented in a fixed point DSP TMS320F2812 with a clock frequency of 150 MHz using the structure described in Table 1. The bus voltage was set to 550 V through a power dc source and the applied phase voltage was 100 Vrms.

Fig. 8*a* shows the applied three-phase voltage, which is 100 Vrms per phase, with a 50 Hz fundamental frequency and a THD = 4%. In Fig. 8*b* the injected phase currents for the proposed sensorless scheme are shown, along with one of the grid phase voltages, which is included to show that the current effectively results in phase with the phase voltage. As in the simulations, the reference current gain goes from zero to 0.07 A/V, and as the figure shows, the startup transient and steady-state behaviours of the implemented controller match those of the simulated one (for the grid voltage of Table 2(a)), which validates the proposal. The steady-state currents result of 7 Arms, as expected, and have a THD = 1.8%, showing the effectiveness of the sensorless strategy. Also, in this figure, the steady-state phase difference between the shown grid voltage (channel 1) and its corresponding current (channel 2) results approximately 0°, showing unity power factor. Finally, Fig. 8*c* shows the measured grid voltage $v_{sa}(k-1)$ (top) along with the estimated grid voltage $\hat{\bar{v}}_{sa}$ (bottom) computed through (15). Both signals were measured from the filtered PWM outputs of the DSP, which were filtered with an RC low pass filter with cutoff frequency of 2340 Hz. As the figure shows, their root mean square (rms) values are 1.306 and 1.281 Vrms respectively, which implies that there is an estimation error of less than 2%.

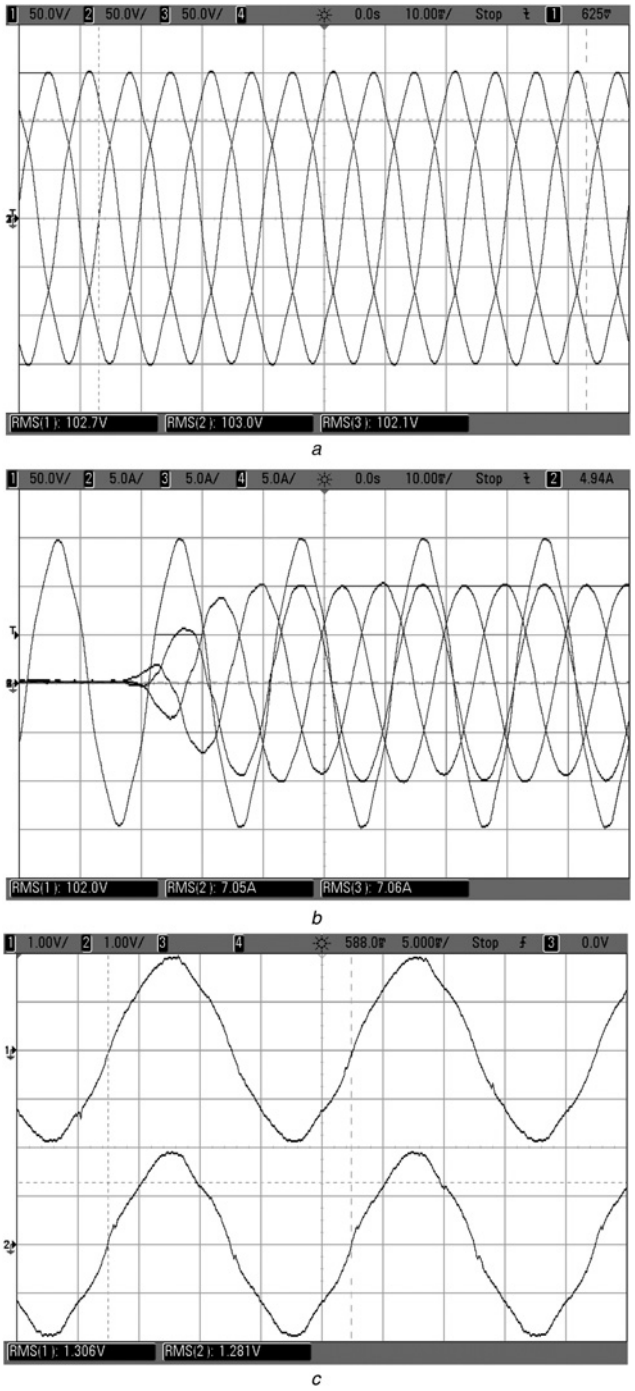

Fig. 8 *Experimental results (horizontal: 10 ms/div)*

a Grid phase voltage (50 V/div and THD = 4%)
b Phase currents (5 A/div and THD = 1.8%) and v_{sa} (50 V/div)
c Measured grid phase voltage (horizontal: 5 ms/div) $v_{sa}(k-1)$ (top, 1.306 Vrms) and estimated grid phase voltage $\hat{v}_{sa}(k-1)$ (bottom, 1.281 Vrms)

Therefore this figure shows that (15) can be used to estimate the grid voltage, with a reasonable precision, for its use in anti-islanding algorithms.

7 Conclusions

This paper proposes a method to modify a ROGI-based current controller allowing it to become grid voltage sensorless. By taking advantage of the controller structure, this improvement is merged seamlessly with the original controller, requiring no additional states and very few additional operations, which keeps the computational burden of the whole controller to a minimum. This allows its easy integration into low cost DSPs. The proposed hardware simplification allows one to obtain a cheaper implementation and also a more reliable scheme. The proposal is validated through simulation and experimental results.

8 References

1 Jin, T., Jimenez, J.A.: 'Review on planning and automation technologies for distributed generation systems'. IEEE Conf. on Automation Science and Engineering, 2010, pp. 269–274. 10.1109/COASE.2010.5583986
2 Balaguer, I.J., Lei, Q., Yang, S., Supatti, U., Peng, F.Z.: 'Control for grid-connected and intentional islanding operations of distributed power generation', *IEEE Trans. Ind. Electron.*, 2011, **58**, (1), pp. 147–157
3 Zhou, T., Francois, B.: 'Energy management and power control of a hybrid active wind generator for distributed power generation and grid integration', *IEEE Trans. Ind. Electron.*, 2011, **58**, (1), pp. 95–104
4 Nian, H., Zeng, R.: 'Improved control strategy for stand-alone distributed generation system under unbalanced and non-linear loads', *IET Renew. Power Gener.*, 2011, **5**, (5), pp. 323–331
5 Shen, J.M., Jou, H.L., Wu, J.C.: 'Transformer-less three-port grid-connected power converter for distribution power generation system with dual renewable energy sources', *IET Power Electron.*, 2012, **5**, (4), pp. 501–509
6 Abdel-Rady Ibrahim Mohamed, Y., El-Saadany, E.F., Salama, M.: 'Adaptive grid-voltage sensorless control scheme for inverter-based distributed generation', *IEEE Trans. Energy Convers.*, 2009, **24**, (3), pp. 683–694
7 Ahmed, K.H., Massoud, A.M., Finney, S.J., Williams, B.W.: 'Autonomous adaptive sensorless controller of inverter-based islanded-distributed generation system', *IET Power Electron.*, 2009, **2**, (3), pp. 256–266
8 Rodriguez, A., Giron, C., Rizo, M., Saez, V., Bueno, E., Rodriguez, F.J.: 'Comparison of current controllers based on repetitive-based control and second order generalized integrators for active power filters'. 35th Annual Conf. of IEEE Industrial Electronics, 2009, pp. 3223–3228. 10.1109/IECON.2009.5415213
9 Ahmed, K.H., Massoud, A.M., Finney, S.J., Williams, B.W.: 'Sensorless current control of three-phase inverter-based distributed generation', *IEEE Trans. Power Del.*, 2009, **24**, (2), pp. 919–929
10 Leon, A.E., Solsona, J.A., Valla, M.I.: 'Control strategy for hardware simplification of VSC-based power applications', *IET Power Electron.*, 2011, **4**, (1), pp. 39–50
11 Mohamed, Y.A.R.I., El-Saadany, E.F.: 'A robust natural-frame-based interfacing scheme for grid-connected distributed generation inverters', *IEEE Trans. Energy Convers.*, 2011, **26**, (3), pp. 728–736.
12 Busada, C.A., Gomez-Jorge, S., Leon, A.E., Solsona, J.A.: 'Current controller based on reduced order generalized integrators for distributed generation systems', *IEEE Trans. Ind. Electron.*, 2012, **59**, (7), pp. 2898–2909
13 Leonhard, W.: 'Control of electrical drives'(Springer, Germany, 1996, 2nd edn.)
14 Martin, K.W.: 'Complex signal processing is not complex. Circuits and systems I: regular papers', *IEEE Trans.*, 2004, **51**, (9), pp. 1823–1836
15 Francis, B.A., Wonham, W.M.: 'The internal model principle for linear multivariable regulators', *Appl. Math. Optim.*, 1975, **2**, (2), pp. 170–194
16 Holtz, J.: 'Sensorless control of induction motor drives', *Proc. IEEE*, 2002, **90**, (8), pp. 1359–1394

9 Appendix

9.1 Controller structure

The controller gains are found using the LQR method with the parameters R and $\boldsymbol{Q}$ shown in Table 1, where diag() represents a matrix whose main diagonal elements are those of the vector in square brackets.

doi: 10.1049/iet-pel.2012.0329

9.2 Transfer function

The open-loop state variable description of the system shown in Fig. 5 is given by

$$\boldsymbol{x}(k+1) = \boldsymbol{A}\boldsymbol{x}(k) + \boldsymbol{B}\vec{u}_c^{\alpha\beta}(k) + \boldsymbol{B}_v\vec{v}_s^{\alpha\beta}(k) \tag{17}$$

where

$$\underbrace{\begin{bmatrix} 1 & \frac{d_2 T_s}{L} & 0 & \cdots & 0 \\ 0 & 0 & 0 & \cdots & 0 \\ 1 + g\frac{\hat{L}}{T_s}\left(e^{j\omega_o T_s} - 1\right) & -gd_2 & e^{j\omega_o T_s} & \cdots & 0 \\ \vdots & \vdots & \vdots & \ddots & 0 \\ 1 & 0 & 0 & 0 & e^{jN\omega_o T_s} \end{bmatrix}}_{\boldsymbol{A}}$$

$$\underbrace{\begin{bmatrix} \frac{d_1 T_s}{L} & 1 & -gd_1 & \cdots & 0 \end{bmatrix}^T}_{\boldsymbol{B}}; \underbrace{\begin{bmatrix} -\frac{T_s}{L} & 0 & 0 & \cdots & 0 \end{bmatrix}^T}_{\boldsymbol{B}_v}$$

the state vector is $\boldsymbol{x} = \left[\vec{i}^{\alpha\beta}\, \vec{u}_d^{\alpha\beta}\, \vec{y}_1\, \vec{y}_{-1} \ldots \vec{y}_N\right]^T$, where y_h, $h \in \mathbb{Z}$ is the output of each ROGI before multiplying it for its respective gain K_h. The closed-loop response of this system is obtained computing

$$\boldsymbol{x}(k+1) = \boldsymbol{A}_{cl}\boldsymbol{x}(k) + \boldsymbol{B}_v\vec{v}_s^{\alpha\beta}(k) \tag{18}$$

where

$$\boldsymbol{A}_{cl} = \boldsymbol{A} - \boldsymbol{B}\left[\left(K_p + g\frac{\hat{L}}{T_s}K_1\right)K_d K_1 K_{-1} \cdots K_N\right]$$

Finally, the transfer function relating the current with $\vec{v}_s^{\alpha\beta}$ is given by

$$G(z) = \frac{\vec{i}^{\alpha\beta}(z)}{\vec{v}_s^{\alpha\beta}(z)} = \boldsymbol{C}\left(z\boldsymbol{I} - \boldsymbol{A}_{cl}\right)^{-1}\boldsymbol{B}_v \tag{19}$$

where $\boldsymbol{I}$ is an identity matrix with the dimensions of $\boldsymbol{A}_{cl}$, and $C = [1\ 0\ 0 \ldots 0]$.